

Role of Cations in the Methane/Carbon Dioxide Partitioning in Nano- and Meso-Pores of Illite using Constant Reservoir Composition Molecular Dynamics Simulation

Narasimhan Loganathan^{1}, A. Ozgur Yazaydin^{1,2}, Geoffrey M. Bowers³, Brice F. Ngouana-Wakou⁴, Andrey G. Kalinichev,⁴ R. James Kirkpatrick^{1,5}*

¹ Department of Chemistry, Michigan State University, East Lansing, Michigan 48824, United States

² Department of Chemical Engineering, University College London, London, WC1E7JE, United Kingdom

³ Department of Chemistry and Biochemistry, St. Mary's College of Maryland, St. Mary's City, Maryland 20686, United States

⁴ Laboratoire SUBATECH (UMR 6457 - Institut Mines-Télécom Atlantique, Université de Nantes, CNRS/IN2P3), 44307, Nantes, France

⁵ Department of Earth and Environmental Sciences, Michigan State University, East Lansing, Michigan 48824, United States

* **Corresponding author e-mail:** naresh20@msu.edu

Abstract

Clay minerals are important components of many shales and other fine grained sedimentary rocks, and interaction of fluid species with their pore systems plays a significant role in controlling their structural and dynamical behavior during oil and gas production from tight reservoirs, in cap rocks of traditional petroleum reservoirs, and in geological carbon sequestration processes. We performed Constant Reservoir Composition Molecular Dynamics (CRC-MD) computer simulations at typical reservoir conditions (323 K and 124 bar) to quantitatively study the partitioning of fluid species between the nano- and meso-pores of clay and a bulk reservoir containing an equimolar mixture of CO₂ and CH₄. The results show that the basal (001) and protonated edge (010) surfaces of illite both demonstrate a strong preference for CO₂ over CH₄ adsorption; that the (001) surfaces show a stronger preference for CO₂ than the (010) surfaces, especially with K⁺ as the exchangeable cation; and that the structuring of the near-surface CO₂ by K⁺ is stronger than by Na⁺. The protonated (010) surfaces have a somewhat greater preference for CH₄, with the concentration near them close to that in the bulk fluid. In contrast, the CH₄ concentration in the first fluid layer at the (001) surface is less than in the bulk, due to the strong preference of that surface for CO₂. The effects of the surfaces on the fluid composition extend to approximately 2.0 nm from them, with the fluid composition at center of the pore becoming essentially the same as the bulk composition at a pore thickness of ~5.7 nm. The CO₂ molecular orientations near the (001) surfaces vary greatly with distance from the surface and are different with K⁺ and Na⁺. Overall, the results confirm the preference of nano- and meso-pores bounded by clay minerals for CO₂ over CH₄ and suggest that injection of CO₂ into tight reservoirs is likely to displace CH₄ into larger pores, thus enhancing its production.

Introduction

Natural gas produced from shale and other tight reservoirs is one of the most important resources for addressing increasing global energy demand, and the injection of carbon dioxide into these reservoirs has significant potential to enhance oil and gas recovery and also to facilitate geological carbon sequestration.¹⁻⁴ Clay minerals are important components of shales and other tight formations,^{5,6} and because the pores in these rocks are so small, interaction of the pore fluids (e.g., H₂O, CO₂ and CH₄) with clay surfaces plays an important role in controlling the structural environments of fluid species, their partitioning between pores of different sizes, and their transport properties.^{7,8} The behavior of water and cations at mineral surfaces and in the nano-scale interlayer galleries of swelling clays has been extensively studied experimentally and by computational molecular simulations,⁹⁻²⁰ and in recent years there has been increasing focus on the partitioning of CO₂ and H₂O into expandable clay interlayers and how factors like mineral composition, cation size and charge, and the saturation state of the fluid phase impact the partitioning characteristics.²¹⁻⁴¹ Mixed CO₂/CH₄ fluids are of significant potential importance, especially near injection wells, but little is known about their mutual behavior in the nano- and meso-pores in shales and other tight formations. Most studies that address CO₂ and CH₄ interactions are focused on their single-component adsorption in the interlayers of expandable clay minerals (smectites), which show a strong preferential adsorption of CO₂ over CH₄.⁴²⁻⁴⁵

There are only a handful of studies investigating CO₂ and CH₄ with the surfaces of other minerals,⁴⁶⁻⁴⁸ including the non-expandable, high charge clay mineral illite,^{8,49} which is a very common component of shales. As for smectites, most studies of illite have focused on the adsorption of single-component fluids species, with the results again demonstrating stronger preference of the basal surfaces for CO₂ relative to CH₄.⁴⁶⁻⁵⁰ Grand Canonical Monte Carlo

(GCMC) simulations of Zhang et al.⁴⁷ showed that the interaction between K^+ on the basal surface and CO_2 plays an important role in the adsorption of CO_2 and that the strength of this interaction decreases with increasing pressure. Similar GCMC studies by Chen et al.⁴⁶ suggested that the quadrupole moment of the CO_2 molecules could contribute to their interaction with the oxygen atoms of the basal surfaces of illite. Gibbs Ensemble Monte Carlo (GEMC) simulations of mixed CO_2/CH_4 fluids interacting with illite basal surfaces by Chong et al.⁴⁸ showed that CO_2 strongly interacts with the surface, that the CO_2 adsorption increases with decreasing CH_4 content in the bulk fluid, and that the surface sorption increases linearly at low pressures (<20 MPa) but reaches a plateau at higher pressures. A recent experimental sorption study by Hwang et al.⁵⁰ also shows stronger interaction between illite and other clay minerals with CO_2 than with CH_4 at $50^\circ C$ and pressures up to 30 MPa. To our knowledge, there have been no studies of the impact of pore thickness (distance between the average positions of the centers of basal surface oxygen atoms forming the pore as shown in Figure 1) and different surface cations on the interaction of CO_2 and CH_4 with illite,⁴²⁻⁵⁰ nor have there been any systematic studies of the protonated surfaces of the T-O-T layer broken edge sites, which can contribute significantly to the total surface area of shales. However, recent experiments of Wan et al.⁴⁹ allowed them to hypothesize that the frayed edges of non-swelling clays may be responsible for the unexpectedly high CO_2 uptake by such clays.

We recently investigated the effect of pore thickness and edge site vs. basal surface on the CO_2/CH_4 partitioning and fluid structure on finite sized Na-montmorillonite surfaces using Constant Reservoir Composition Molecular Dynamics (CRC-MD) simulations.⁵¹ The results showed that CO_2 adsorption dominates at both the basal and broken edge surfaces and that the CO_2/CH_4 ratio in the pore fluid approaches the bulk value with increasing distance from the surface. In this paper, we present the results of CRC-MD simulations of the partitioning and

structural environments of CO₂ and CH₄ in nano- and meso-pores of illite with K⁺ or Na⁺ as surface charge-compensating ions, quantifying also the differences in near-surface structure between basal and broken edge surfaces. The results show that the partitioning of CO₂ and CH₄ between the bulk fluid (representative of the composition in large interparticle pores) and the nano- and meso-pores is greatly influenced by the pore thickness and the nature of the charge balancing cations. Irrespective of the cation, the basal and broken edge surfaces show a stronger preference for CO₂ relative to CH₄, and the preference is substantially greater than for Na-montmorillonite.⁵¹

The main objective of our study is to understand the influence of the exchangeable cation in determining the partitioning of supercritical CO₂ and CH₄ in nano- and meso-confined pores of the common clay mineral illite. A series of CRC-MD simulation were performed with an equimolar mixture of CO₂/CH₄ at 323 K and 124 bar to address the partitioning behavior using illite particles with pore thickness ranging from 0.3 nm to 7.6 nm. In the following section, we introduce the CRC-MD technique, describe how the simulation cell and finite size illite particle is constructed, and then describe the simulation details used to carry out this study. In the results and discussion section, we present the partitioning of CO₂ and CH₄ fluids with increasing pore thickness, discuss their structure, coordination with the exchangeable cations and their orientation near the pore surfaces. In addition, the effect of broken edge sites in altering the adsorption structure of the fluid species is also investigated. The key important outcomes are summarized in the conclusion section.

Methods

CRC-MD is a novel molecular modeling technique that maintains a constant composition of the fluid in designated volumes external to the pore (Figure 1) by applying self-adjusting bias

forces. This method has been used previously to maintain constant chemical potentials of the fluid species in modelling growth of urea crystals^{52,53} and to create a concentration gradient across a membrane (concentration gradient driven MD) for modelling gas separation and transport of mixed fluid species.⁵⁴ We have previously discussed the advantages of CRC-MD over hybrid MC/MD approaches, such as dual control volume grand canonical molecular dynamics, in maintaining constant external fluid composition and for modeling dense fluids in which Monte Carlo exchanges are difficult.^{54,55} Here, each simulation cell consists of a bulk fluid reservoir, two bias force regions, two composition control regions, two transition regions, and the illite + pore assemblage in the center (Figure 1). The concentration of the fluid species in the control regions is maintained at target values by forces in the bias force regions. These bias forces act in such a way that if the instantaneous concentration of a given species in a control region is different from the target concentration then molecules are moved from the control region to the reservoir or moved into the control region from it. A detailed explanation of the functional forms of the bias forces and how they work can be found in the supporting information and elsewhere.^{52,54} Our simulations used finite size illite particles with pore thickness between 0.3 and 7.6 nm that were placed between the two external reservoirs with an equimolar CO₂/CH₄ ratio (Figure 1). The pore thickness is defined as the distance between the average positions of the centers of basal surface oxygen atoms confining the pore (Figure 1b). The reservoir regions contain equimolar mixtures of CO₂ and CH₄. Thus, both the basal and protonated broken edge surfaces were investigated simultaneously. Surfaces with both K⁺ and Na⁺ were modeled to investigate the effect of CO₂ solvation energy of the charge-balancing cation on the fluid behavior. Illite has K⁺ as its most abundant interlayer cation, but it is possible that other cations could exchange onto external surface sites, especially if the fluid is a NaCl-rich brine.^{56,57} The pore dimensions used in our study

represent those of interparticle pores between finite sized illite particles. The interparticle pores can vary from few nanometers to few hundreds of nanometers, depending upon the arrangement of clay particles.⁵⁸ Based on our previous studies with montmorillonite,⁵¹ the largest pore thickness (7.6 nm) used in our study is sufficient to depict both the near surface structure and the fluid structure and composition far from the surface.

The finite-size illite particle is based on ideal muscovite with the total structural charge reduced 20% by including less tetrahedral Al³⁺ for Si⁴⁺ substitution. Illite develops its permanent negative structural charge principally by isomorphic substitution of Al³⁺ for Si⁴⁺ in the tetrahedral sheet. The structural formula of our model illite is M⁺_{1.6}(Si_{6.4}Al_{1.6})(Al₄)O₂₀(OH)₄.⁵⁹ The distribution of the Al³⁺ for Si⁴⁺ isomorphic substitution has a quasi-disordered pattern that is in accordance with Lowenstein's rule, which forbids tetrahedral Al-O-Al linkages.⁶⁰ The simulated illite particle has finite lateral dimensions of ~7.30 nm × 4.14 nm along the crystallographic *a* and *b* axes, with an orthorhombic unit cell. To construct the finite size particle, the illite structure was cleaved along (010), creating broken edge sites on that surface. The dangling bonds of the tetrahedral Al³⁺ and Si⁴⁺ sites on the broken edges were then saturated with single OH⁻ groups, whereas the dangling octahedral Al³⁺ sites were saturated with 1 OH⁻ group and 1 H₂O molecule, resulting in a charge-neutral edge surface. This illite particle has one (010) surface exposing some tetrahedral Al³⁺ sites and one that exposes only tetrahedral Si⁴⁺ sites. Further details about the edge site structures can be found elsewhere.⁵¹

The illite particle consists of three T-O-T layers and two anhydrous interlayers. It exposes two external basal (001) surfaces to the pore. The total simulated model including the volumes occupied by the fluid has lateral dimensions of 30.0 nm × 4.14 nm (Figure 1). Because of the 3-dimensional periodic boundary conditions employed, only the broken (010) edge surface plane

and the basal surfaces bounding the pore are exposed to the fluid. The pore thickness between the external basal surfaces was varied from 0.3 to 7.6 nm. For models with pore thickness less than 1.0 nm, the charge compensating cations were placed initially at the midplane of the pores. At larger pore thicknesses, these ions were placed 0.5 nm from each external basal surface, thereby allowing the cations to choose their preferred adsorption sites during the simulation run. The fluid molecules (CO_2 and CH_4) were initially placed external to the illite particle at distances $>\sim 3.0$ nm from the two broken (010) surfaces. The total number of fluid molecules in the entire simulation cell increases with increasing pore thickness in order to maintain the desired target densities in the control region. The non-swelling illite interlayers contain only K^+ ions.

The partitioning of CO_2/CH_4 and density profiles for each species near the particle surfaces are analyzed in three different dimensions: (i) normal to the basal (001) surfaces bounding the pore (z direction); (ii) parallel to the broken edges in the transition regions (along the z direction); (iii) normal to the broken (010) edges in the transition region (along the x direction). Similarly, the nominal location of the (010) surfaces is defined as the plane containing the time-averaged positions of the centers of the protonated oxygen atoms on the surface. The orientation of the CO_2 molecules and the nearest neighbor coordination among different species on the basal surfaces are analyzed with radial distribution functions and probability density plots. In addition, the total fluid density in the pores confined by basal (001) surfaces is calculated for all pore thickness. In addition, we also calculate the total fluid density which corresponds to the average total number of fluid species ($\text{CO}_2 + \text{CH}_4$) over volume within the illite pore region. Note, the volume of finite sized illite pore region is computed by considering the average positions of the centers of basal (001) surface oxygen atoms bounding the pore in z -direction and time-averaged positions of the protonated oxygen atoms on either sides of the particle as the lateral boundary limit along x -

direction (~7.3 nm), in contrast to actual simulated cell dimensions along y-direction (4.14 nm). Further details about the analysis methods are described elsewhere.^{34-36,41,51}

Molecular dynamics simulations in the canonical *NVT* ensemble at 323 K were performed using the LAMMPS simulation package.⁶¹ A Nose-Hoover thermostat was used to control the temperature.⁶² The interatomic interactions for the illite were obtained from the *ClayFF* force field,⁶³ and the parameters for the broken edge sites were obtained from newly developed metal-O-H bending potentials consistent with *ClayFF*.^{64,65} The EPM2⁶⁶ and TraPPE-UA⁶⁷ interaction potentials were used to represent the CO₂ and CH₄ molecules, respectively. More details about the interaction potentials can be found in the Supporting Information. Three-dimensional periodic boundary conditions were employed. A cutoff of 1.40 nm was used to compute short-range non-electrostatic interactions, and the long-range electrostatic interactions were computed using the particle-particle-particle-mesh (PPPM) summation algorithm with an accuracy of 10⁻⁶.⁶⁸ A time step of 1 fs was used to integrate the equations of motion. Each system was initially equilibrated for 15 ns, followed by another 2 ns of data production with the atomic coordinates recorded every 10 fs. Importantly, the movement of the clay layers with respect to each other was restricted by fixing the positions of 18 octahedral Al³⁺ atoms in the simulated illite structure (6 per each TOT layer).

A modified version of the PLUMED 2.3.0 plugin was used to apply the bias forces to maintain the fluid composition in the control regions.⁶⁹ The target CO₂ and CH₄ densities in the control regions were set to 2 CO₂ and 2 CH₄ molecules/nm³. At the simulated temperature of 323 K, the reference target densities of fluid species in the control regions correspond to a total fluid pressure of 124 bars, based on the Peng-Robinson equation of state.⁷⁰ These temperature and pressure conditions are relevant to the upper part of the Earth's crust and petroleum reservoirs.

The width of the transition regions, control regions and the bias force regions were set to 3.0 nm, 3.0 nm and 0.30 nm, respectively. The target compositions of the fluid species, i , in the control regions were maintained using the force constants $k_i^L = k_i^R = 5000 \text{ kJ}\cdot\text{nm}^3/\text{mol}$, which are placed at the center of the bias force regions. The compositions in the control regions were monitored at intervals of 0.5 ps during the entire simulation. This procedure maintained the desired composition in the control regions very well (Figure S1).

Results and Discussion

Pores Bounded by Basal Surfaces

The mole fraction and number densities of CO_2 and CH_4 molecules in the pores bounded by the basal (001) surfaces vary greatly with pore thickness (Figures 2a and 2b). For both the K- and Na-surfaces, the total fluid density $\left(\frac{N_{(\text{CO}_2+\text{CH}_4)}}{\text{Volume of illite pore region}}\right)$ increases rapidly from a pore thickness of $\sim 0.4 \text{ nm}$, reaches a plateau at pore thickness between 1.0-1.5 nm, and then decreases with increasing pore thickness. There is a second plateau between 2.5-3.5 nm in the mole fractions for both models. With both cations, at pore thickness less than 1.0 nm CO_2 saturates the pore, and there is a negligible amount of CH_4 . The CH_4 molecules that do appear in the pore are concentrated predominantly at the pore openings of the finite illite particle. The CO_2/CH_4 ratio does not depend significantly on the exchangeable cation, decreases with increasing pore thickness, and slowly approaches but does not reach the bulk ratio of 2.0 molecules/ nm^3 even at a pore thickness of 7.6 nm. The large CO_2/CH_4 ratio and its decrease with increasing pore thickness are in good agreement with previous simulations that indicate a favorable energetic interaction of CO_2 molecules but not for CH_4 molecules with the basal surfaces of illite,⁴⁶ and also parallel the behavior of these species in pores bounded by the smectite clay montmorillonite.⁵¹

With surface Na^+ , the results here show that significant CH_4 content occurs at 0.75 nm pore thickness and that its mole fraction increases almost linearly until the first plateau region starting at pore thickness of 1.26 nm is reached. In contrast, with surface K^+ , significant amounts of CH_4 do not occur until a pore thickness of 1.0 nm. As a result, the CO_2/CH_4 ratio with K^+ is approximately twice that with Na^+ at a 1.0 nm pore thickness. At pore thickness > 1.0 nm, the CH_4 content with K^+ increases gradually, reaches a plateau, and approaches the value with Na^+ at a pore thickness of 2.2 nm. The number density of CO_2 molecules is greater in the illite-bounded pore than in the control region at all pore thicknesses studied, with maximum values of 9.0 and 10.0 at a 1.0 nm pore thickness with K^+ and Na^+ , respectively (Figure 2b). At larger pore thickness ($z > 2.5$ nm), the number density of CO_2 decreases significantly, in contrast to CH_4 which does not change much. Unlike CO_2 , the number density of CH_4 never surpasses the value of 2 molecules/ nm^3 in the control region.

These results are in good agreement with previous GCMC simulation studies of K-illite in contact with pure CO_2 or pure CH_4 at similar thermodynamic conditions^{46,47} and are probably due to the favorable K^+ - CO_2 solvation energies.⁷¹ These observed changes strongly suggest that pores with thicknesses of 1 to a few nm bounded by clay surfaces have a significant preference for adsorption of CO_2 relative to CH_4 , with the greatest preference exhibited by nano-pores (< 1 nm). Our results are also consistent with adsorption energetics and gas sorption studies that show the clay minerals prefer CO_2 over CH_4 under anhydrous conditions.⁵⁰ Importantly, our results demonstrate that the exchangeable surface cations affect CO_2/CH_4 partitioning only up to pore thickness of few nm (~ 4).

The probability density profiles (PDPs) of CO_2 and CH_4 normal to the (001) illite surfaces show that the structuring of the fluid species near the pore surfaces is greatly different with K^+

compared to Na^+ as the charge-balancing surface cation (Figures 3 and Figure S2). With K^+ , the PDPs of CO_2 show 3 discernable layers extending up to ~ 1.8 nm from the basal surfaces along with a shoulder near 0.4 nm. With Na^+ there are only 3 distinguishable layers. With both K^+ and Na^+ , the PDPs of CH_4 show 3 layers extending up to 1.5 nm from the surface. At larger pore thicknesses, the CO_2/CH_4 ratios are large near the surface, gradually decrease with increasing distance from the surface, and reach the composition of the control volume at about 2.2 nm away from the surface. With K^+ at a pore thickness of 0.78 nm, there is a broad peak for CO_2 and a poorly resolved CH_4 maximum near the middle of the pore (Figure 3). In contrast, with Na^+ , there are well-defined peaks for CO_2 near each pore surface, a well-defined peak in the center of the pore, and a CH_4 density maximum near the center of the pore that is broader than with K^+ (Figure 3). At a pore thickness of 0.94 nm, there are well-defined first layers of CO_2 and CH_4 molecules at about 0.3 nm from the surfaces with both K^+ and Na^+ , but the CH_4 density is substantially smaller with K^+ than with Na^+ . In addition, there is a well-defined peak for CO_2 in the center of the pore with K^+ , but not Na^+ . At 1.09 nm, CO_2 molecules form two layers at each surface with both K^+ and Na^+ , but the second peak with Na^+ near 0.4 nm is a less well resolved shoulder. CH_4 forms layers about 0.35 - 0.38 nm from the surfaces for both compositions, with those of the Na^+ system being better resolved. At a pore thickness of 1.24 nm, a third peak for CO_2 and a second peak for CH_4 near 0.63 nm begin to form the center of the pore. Importantly, the intensity of the second CH_4 peak is greater than that of the first peak with both K^+ and Na^+ . At 1.56 nm there are three peaks or shoulders for CO_2 and two peaks for CH_4 for both K^+ and Na^+ systems.

At pore thicknesses between 1.56 and 2.65 nm, in addition to these peaks, with both K^+ and Na^+ on the surface, there are the same near-surface peaks as at smaller pore thicknesses along with a flat distribution for both fluid species in the center of the pores. The CH_4 density in the pore

center is very similar to that in the control region, whereas the CO₂ densities are much greater. At pore thickness > 2.65 nm with K⁺, there is a significant change in the structuring of the CO₂ molecules, but not the CH₄ molecules, near the pore surfaces (Figures 3 and S2). The second peak of CO₂ becomes a shoulder on the peak nearest the surface, most likely due to redistribution of CO₂ between the near surface layers. In addition, the CO₂ densities in the middle of the pore gradually decrease towards the composition in the control volume. With both K⁺ and Na⁺ as the charge-balancing surface cation, by 5.70 nm the fluid structuring near the surfaces does not change with further increasing pore thickness, and the CH₄ and CO₂ densities are essentially the same in the center of the pore. At the largest pore thickness studied (7.68 nm), with both K⁺ and Na⁺ the CO₂ peak maxima are at 0.3, 0.67 and 1.03 nm from the pore surfaces and there is a shoulder at 0.45 nm only with K⁺. In contrast, the peak maxima for CH₄ occur at 0.33 and 0.65 nm with both K⁺ and Na⁺ as surface cations, but the intensity of the CH₄ peak at 0.33 nm is substantially lower with K⁺ than with Na⁺. The CH₄ and CO₂ concentrations in the centers of the pores are very close to the composition in the control volume (2 molecules/nm³). The CO₂ and CH₄ PDPs with K⁺ here are substantially different than those for an equimolar CH₄/CO₂ ratio in the GEMC studies of Chong et al.,⁴⁸ mostly likely due to their use of cation substitution on the octahedral sites, which is not commonly found in natural illites, in contrast to the tetrahedral substitutions used in our work. Their models also had a lower structural charge than ours. Similarly, we attribute the difference in the PDPs of the 1st layer CH₄ with Na⁺ here compared to Na-montmorillonite under the same thermodynamic conditions and fluid composition to the lower structural charge and the octahedral substitution in the montmorillonite.⁵¹

Irrespective of the exchangeable surface cation, the differences in the structuring of CO₂ and CH₄ near the pore surfaces in our simulations are due to differences in their interaction with

the basal surface oxygen atoms.⁵¹ Clay surfaces clearly prefer CO₂ to CH₄. The differences in fluid structuring with K⁺ and Na⁺, however, are due to differences in the solvation energies of the cations by CO₂.⁷⁰ Because K⁺ has greater affinity towards CO₂ than Na⁺, the increased number of CO₂ molecules in the fluid layer nearest the surface with K⁺ restricts CH₄ molecules from entering that layer. As with Na-montmorillonite,⁵¹ there are two CO₂ coordination environments on the (001) surface: (i) one O_{CO2} located above the center of a ditrigonal cavity and the other O_{CO2} located 0.3 nm above a Si/Al tetrahedron and (ii) the C_{CO2} relatively close to a tetrahedral Si/Al site (0.45 nm). This fluid structuring is also similar to that of CO₂ in the interlayers of smectites.^{34-36,38} In contrast, the absence of a well-resolved CH₄ peak in the first layer here shows negligible coordination with the surface. These conclusions are in good agreement with the structure of CH₄ in nano- and mesopores of montmorillonite-bounded pores under identical thermodynamic conditions.⁵¹

The PDPs of the exchangeable cations (K⁺ and Na⁺) are greatly influenced by increasing pore thickness. At collapsed basal spacings (Figure 3), the K⁺ ions are located at the mid-plane of the pore, whereas Na⁺ shows two peaks at 0.13 nm from each surface. At all other pore thicknesses, there are two peaks for K⁺ and Na⁺, but their positions are very different. The dominant peak for K⁺ is at 0.17 nm, and the K⁺ ions are located above the centers of ditrigonal cavities. The minor K⁺ peak at 0.25 nm is located above Al tetrahedra. In contrast, due to its smaller size the dominant Na⁺ peak is at 0.05 nm, and the ions are located at the centers of ditrigonal cavities sharing the same plane as the basal (001) oxygen atoms. The second Na⁺ peak is at 0.20 nm, and these ions are located near the Al tetrahedra. These results are in good agreement with previous simulation studies of Na⁺ on the surfaces of hectorite.¹³ Similarly, the location of the highest K⁺ peak (at ~0.17 nm) is in good agreement with the results of previous simulation studies of muscovite.⁷²

The radial distribution functions (RDFs) and running coordination numbers (RCNs) show clearly that both the K^+ and Na^+ ions are essentially all in inner sphere coordination to the basal oxygen atoms at all pore thickness studied (Figures 4a and 4b). The mean K^+O_b and Na^+O_b interatomic distances are ~ 0.28 and ~ 0.25 nm, respectively, and do not vary with varying pore thickness. Similarly, the cation- O_b RCNs only increase from 5.2 to 6.0 (K^+) and 5.4 to 5.9 (Na^+) with increasing pore thickness. The RDFs for CO_2 show its direct coordination to both cations (Figures 4c and 4d). Irrespective of the pore thickness, the mean interatomic distances between the cations and the nearest O_{CO_2} is ~ 0.30 nm for K^+ and ~ 0.25 nm for Na^+ . Similarly, the cation- O_{CO_2} RCNs are ~ 2.5 for K^+ and ~ 1.6 for Na^+ at all pore thickness. None of the models show significant coordination between CH_4 and the exchangeable surface cations, even for short periods of time (Figures 4e and 4f). The energetically favourable interactions between K^+ and CO_2 , along with the larger ionic radius of K^+ , are responsible for its higher RCN values compared to Na^+ , which are in excellent agreement with the relative CO_2 solvation energies of the ions and the results of our previous studies of smectites.^{35,71} The interatomic distances between K^+ and O_b and O_{CO_2} are in excellent agreement with previous simulation studies at ambient conditions (298K).^{47,72}

The distribution of CO_2 molecular orientations in the first 3 layers near the (001) surfaces are quite different with K^+ and Na^+ as exchangeable cations, but both change from quite structured in the first layer to nearly isotropic in the third layer. The changes with changing pore thickness show the greatest structural variability at small pore thicknesses (Figure 5). With both K^+ and Na^+ , the CO_2 molecules in the first layer (1L) are oriented predominantly parallel to the basal surface and undergo librational motion around an axis perpendicular to their O-C-O vector (Figures 5a and 5b). The values of 0 and ± 1 for $\cos\theta_{CO_2}$ correspond to CO_2 orientations parallel and perpendicular to the plane of the basal surface. The broader distributions in the first layer (1L) with

Na⁺ show that the CO₂ molecules are in less restricted environments than with K⁺. The more restricted orientations with K⁺ and the preferred orientation of the CO₂ molecules in the first fluid layer with one of their O-atoms towards the K⁺ ions are well illustrated by the surface maps for the two 7.68 nm illite models shown in Figure 6. These maps are sums of 2000 individual snapshots in the production runs. Importantly, these orientation distributions at pore thicknesses <1.0 nm are in reasonable agreement with the calculated distributions in the interlayers of smectites.^{34-36,41} The CO₂ orientation distributions in the second layer (2L) are very different with both K⁺ and Na⁺ (Figure 5c and 5d), although both have much broader angular distributions than in the first layer. With K⁺, the CO₂ molecules undergo larger wobbling motion of their primary axis with respect to the illite surface normal than in 1L and have distributions with average values of +0.7 (45°) and -0.7 (135°), along with a small fraction parallel to the surface. In contrast, with Na⁺ at the surface, the maxima in the distributions of the CO₂ orientations are parallel (0) and perpendicular (±1) to the basal surfaces. These two orientations suggest that CO₂ molecules experience both orientations, with the perpendicular orientation much more probable. In the third layer, with both K⁺ and Na⁺ on the surface, the distributions are nearly isotropic and almost identical (Figures 5e and 5f). The differences between the K⁺-and Na⁺-models in the first two layers are due to the Na⁺ ions being pinned at the center of the ditrigonal cavities at the level of the basal oxygen atoms and the K⁺ ions being on average 0.17 nm above basal oxygens. In addition to the preference of CO₂ for K⁺ relative to Na⁺, the position of K⁺ limits the accessible, near-surface space for dynamic CO₂ reorientation and restricted motion extends into 2L (Figure 5b).

Broken Edge Surfaces

The PDPs of CO₂ and CH₄ on the surfaces of the broken edge (010) surfaces of the clay layers are qualitatively similar to those on the basal (001) surfaces at large pore thicknesses (Figure

7) but are quantitatively different. For both CO₂ and CH₄, the concentrations in the near-surface layers on the (010) surfaces are greater than in the control volumes, the concentration of CO₂ is greater than that of CH₄, but the CO₂ concentrations are less and the CH₄ concentrations more than on the (001) surfaces. This latter result clearly indicates that the affinity of CO₂ for the protonated edge sites is weaker than for the basal surfaces. This result is expected, because with the charge-neutral protonation state of the modeled (010) surfaces, there are no exchangeable cations on them, and on the (001) surface interactions between CO₂ and the exchangeable cation appear to play a significant role. On the (010) surfaces, CO₂ shows two well defined layers centered at ~0.30 and ~0.65 nm from the surface, with a poorly resolved shoulder at ~0.15 nm. CH₄ shows two layers centered at 0.36 and 0.65 nm, the same distances as on the basal (001) surfaces, corroborating the idea that CH₄ adsorption on silicate surfaces is non-specific. The exchangeable cation has no effect, with the location of the peak maxima and the concentrations essentially identical with both K⁺ and Na⁺. Similarly, the distributions are essentially identical for surfaces containing both tetrahedral Al and Si sites and those with only Si, as we observed previously for montmorillonite with no tetrahedral Al and mixed octahedral Al and Mg sites.⁵¹ As at the basal (001) surfaces, the increased concentrations with respect to the control volume extend to ~2.0 nm from (010) surfaces (Figures 7c and 7d). We observe that CO₂ molecules in the shoulder region (~0.15 nm) are adsorbed in narrow channels closer to the fluctuating hydroxyl groups and H₂O molecules on the (010) edge sites. Figure 7e (a sum of 2000 individual snapshots in the production run) clearly shows that the volumes probed by CO₂ molecules are dictated by the orientation of the (010) edge site groups.

As expected, the fluid structure normal to the (010) edge surfaces is independent of the pore thickness, since these surfaces face the transition region and are the same for each pore thickness investigated. Similarly, the PDPs of the total CO₂ within 1.5 nm of the (010) surfaces

also demonstrate the preference these surfaces for CO₂ (Figures 7a and 7b). In contrast, there is no significant difference in the CH₄ concentration in this region and in the control regions. Notably, the composition of the fluid directly above the center of the 7.68 nm pore is the same as in the control region, as also observed in our previous simulations with montmorillonite.⁵¹ This result suggests that the distribution of fluid species near broken edges of clay particles is determined primarily by the nature of the cleaved surface and associated protonation state and is not greatly affected by the clay structural charge and the nature of the exchangeable cations.

Conclusions

Computational molecular modeling of the interactions of an equimolar mixture of CO₂ and CH₄ with the external (001) and protonated (010) surfaces of illite with both K⁺ and Na⁺ as the exchangeable cation on the (001) surfaces performed at a temperature of 323 K and a total fluid pressure of 124 bars shows that these surfaces have a strong preference for CO₂ over CH₄ as observed in the adsorption energetics and gas sorption experiments.⁵⁰ In general, the results are similar to those of analogous calculations for the smectite mineral Na-montmorillonite.⁵¹ Together these results suggest that small pores in shales and other tight reservoir rocks bounded by clay minerals greatly prefer CO₂ and thus that injection of CO₂ into such rocks is likely to displace CH₄ from small pores and thereby enhance natural gas production. The calculations were performed using Constant Reservoir Composition Molecular Dynamics (CRC-MD), which is proving to be a very useful technique to model partitioning of fluid species between a bulk reservoir and nano- and meso-pores if the fluid species are mutually soluble. Other important results include the following.

1) The (001) surfaces show a stronger preference for CO₂, especially with K⁺ as the exchangeable cation. The solvation energy of K⁺ by CO₂ is known to be stronger than that of Na⁺.⁷¹

2) The protonated (010) surfaces have a somewhat greater preference for CH₄ than the (001) surfaces, with the concentration near the surface close to that in the bulk fluid. In contrast, the CH₄ concentration in the first fluid layer on the (001) surfaces is less than in the bulk.

3) The effects of the surfaces on the fluid composition extend to approximately 2.0 nm from them, and the composition of the fluid in the center of the pore becomes essentially the same as in the bulk at a pore thickness of approximately 5.7 nm.

4) The orientations of the CO₂ molecules near the (001) surfaces vary greatly with distance from the surface and are substantially different for surfaces charge-balanced by K⁺ or Na⁺. Overall, the results confirm the preference of nano- and meso-pores bounded by clay minerals for CO₂ over CH₄. However, this competitive adsorption of CO₂ and CH₄ in illites may vary greatly in the presence of H₂O in natural geological settings, because the hydration behavior of the exchangeable cations varies significantly.⁷³ Understanding these effects is an objective of future work.

Acknowledgements

The authors acknowledge computational resources from the National Energy Research Scientific Computing Center, which is supported by the Office of Science of the U.S. Department of Energy under ECARP No. m1649 and the iCER computational facility at Michigan State University. The work in this manuscript was supported by the Michigan State University Foundation through an MSU Foundation Professorship to R.J.K. A.G.K. and B.F.N-W. acknowledge financial support of the industrial chair “Storage and Disposal of Radioactive Waste” at the IMT-Atlantique, funded by ANDRA, Orano, and EDF, and of the European Union’s Horizon 2020 research and innovation program under grant agreement No. 764810.

Notes

The authors declare no competing financial interest.

Supporting Information

Additional details of the simulation methodology and their functional forms. Concentration variation in the left and right control regions for CO₂ and CH₄ as a function of simulation time in both illite models. Details of the planar atomic density distributions of CO₂ and CH₄ with increasing pore thickness for both K- and Na-illites at 001 basal surfaces.

References

1. Ilgen, A. G.; Heath, J. E.; Akkutlu, I. Y.; Bryndzia, L. T.; Cole, D. R.; Kneafsey, T. J.; Milliken, K. L.; Pyrak-Nolte, L. J.; Suarez-Rivera, R., Shales at all Scales: Exploring Coupled Processes in Mudrocks. *Earth-Science Reviews* **2017**, *166*, 132-152.
2. Pan, Y.; Hui, D.; Luo, P.; Zhang, Y.; Sun, L.; Wang, K. Experimental Investigation of the Geochemical Interactions Between Supercritical CO₂ and Shale: Implications of CO₂ Storage in Gas-Bearing Shale Formations. *Energy Fuels* **2018**, *32*, 1963–1978.
3. Wilkins, R.; Menefee, A. H.; Clarens, A. F. Environmental Life Cycle Analysis of Water and CO₂-Based Fracturing Fluids Used in Unconventional Gas Production. *Environ. Sci. Technol.* **2016**, *50*, 13134-13141.
4. Pei, P.; Ling, K. G.; He, J.; Liu, Z. Z. Shale Gas Reservoir Treatment by a CO₂-Based Technology. *J. Nat. Gas Sci. Eng.* **2015**, *26*, 1595–1606.
5. Gu, M.; Xian, X.; Duan, S.; Du, X. Influences of the Composition and Pore Structure of a Shale on its Selective Adsorption of CO₂ over CH₄. *J. Nat. Gas Sci. Eng.* **2017**, *46*, 296-306.
6. Godec, M.; Koperna, G.; Petrusak, R.; Oudinot, A. Potential for Enhanced Gas Recovery and CO₂ Storage in the Marcellus Shale in the Eastern United States. *Int. J. Coal Geol.* **2013**, *118*, 95-104.
7. Striolo, A.; Cole, D. R., Understanding Shale Gas: Recent Progress and Remaining Challenges. *Energy & Fuels* **2017**, *31*, 10300–10310.
8. Ho, T. A.; Striolo, A. Water and Methane in Shale Rocks: Flow Pattern Effects on Fluid Transport and Pore Structure. *AIChE J*, **2015**, *61*, 2993-2999.
9. Weiss, C. A.; Kirkpatrick, R. J.; Altaner, S. P. Variations in Interlayer Cation Sites of Clay Minerals as Studied by ¹³³Cs MAS Nuclear Magnetic Resonance Spectroscopy. *Amer. Mineral.* **1990**, *75*, 970-982.
10. Bowers, G. M.; Singer, J. W.; Bish, D. L.; Kirkpatrick, R. J. Alkali Metal and H₂O Dynamics at the Clay/Water Interface. *J. Phys. Chem. C* **2011**, *115*, 23395-23407.
11. Weiss, C. A.; Kirkpatrick, R. J.; Altaner, S. P. The Structural Environments of Cations Adsorbed onto Clays – ¹³³Cs Variable-Temperature MAS NMR Spectroscopic Study of Hectorite. *Geochim. Cosmochim. Acta* **1990**, *54*, 1655-1669.
12. Morrow, C. P.; Yazaydin, A. O.; Krishnan, M.; Bowers, G. M.; Kalinichev, A. G.; Kirkpatrick, R. J. Structure, Energetics and Dynamics of Smectite Clay Interlayer Hydration: Molecular Dynamics and Metadynamics Investigation of Na-Hectorite. *J. Phys. Chem. C* **2013**, *117*, 5172-5187.
13. Greathouse, J. A.; Hart, D. B.; Bowers, G. M.; Kirkpatrick, R. J.; Cygan, R. T. Molecular Simulation of Structure and Diffusion at Smectite-Water Interfaces: Using Expanded Clay Interlayers as Model Nanopores. *J. Phys. Chem. C* **2015**, *119*, 17126-17136.
14. Loganathan, N.; Yazaydin, A. O.; Bowers, G. M.; Kalinichev, A. G.; Kirkpatrick, R. J. Structure, Energetics and Dynamics of Cs⁺ and H₂O in Hectorite: Molecular Dynamics Simulations with Unconstrained Substrate Surface. *J. Phys. Chem. C* **2016**, *120*, 10298-10310.

15. Teich-McGoldrick, S. L.; Greathouse, J. A., Colon, C. F.; Cygan, R. T. Swelling Properties of Montmorillonite and Beidellite Clay Minerals from Molecular Simulation: Comparison of Temperature, Interlayer Cation, and Charge Location Effects. *J. Phys. Chem. C* **2015**, *119*, 20880-20891.
16. Loganathan, N.; Yazaydin, A. O.; Bowers, G. M.; Kalinichev, A. G.; Kirkpatrick, R. J. Cation and Water Structure, Dynamics and Energetics in Smectite Clays: A Molecular Dynamics Study of Ca-Hectorite *J. Phys. Chem. C* **2016**, *120*, 12429-12439.
17. Reddy, U. V.; Bowers, G. M.; Loganathan, N.; Bowden, M.; Yazaydin, A. O.; Kirkpatrick, R. J. Water Structure and Dynamics in Smectites: ^2H NMR Spectroscopy of Mg, Ca, Sr, Cs and Pb-Hectorite. *J. Phys. Chem. C* **2016**, *120*, 8863-8876.
18. Bowers, G. M.; Singer, J. W.; Bish, D. L.; Kirkpatrick, R. J. Structure and Dynamical Relationships of Ca^{2+} and H_2O in Smectite/ $^2\text{H}_2\text{O}$ Systems. *Amer. Mineral.* **2014**, *99*, 318-331.
19. Nanda, R.; Bowers, G. M.; Loganathan, N.; Burton, S. D.; Kirkpatrick, R. J. Temperature Dependent Structure and Dynamics in Smectite Interlayers: ^{23}Na MAS Spectroscopy of Na-Hectorite. *RSC Adv.* **2019**, *9*, 12755-12765.
20. Loganathan, N.; Kalinichev, A. G. Quantifying the Mechanisms of Site-Specific Ion Exchange at an Inhomogeneously Charged Surface: Case of Cs^+/K^+ on Hydrated Muscovite Mica. *J. Phys. Chem. C* **2017**, *121*, 7829-7836.
21. Schaef, H. T.; Loring, J. S.; Glezakou, V. A.; Miller, Q. R. S.; Chen, J.; Owen, A. T.; Lee, M.-S.; Ilton, E. S.; Felmy, A. R.; McGrail, B. P. et al. Competitive Sorption of CO_2 and H_2O in 2:1 Layer Phyllosilicates. *Geochim. Cosmochim. Acta* **2015**, *161*, 248-257.
22. Loring, J. S.; Schaef, H. T.; Turcu, R. V. F.; Thompson, C. J.; Miller, Q. R.; Martin, P. F.; Hu, J.; Hoyt, D. W.; Qafoku, O.; Ilton, E. S. et al. In Situ Molecular Spectroscopic Evidence for CO_2 Intercalation into Montmorillonite in Supercritical Carbon Dioxide. *Langmuir* **2012**, *28*, 7125-7128.
23. Loring, J.S.; Ilton, E.S.; Chen, J.; Thompson, C.J.; Martin, P.F.; Benezeth, P.; Rosso, K.M.; Felmy, A.R.; Schaef, H.T. In Situ Study of CO_2 and H_2O Partitioning Between Na-Montmorillonite and Variably Wet Supercritical Carbon Dioxide. *Langmuir* **2014**, *30*, 6120-6128.
24. Loring, J. S.; Schaef, H. T.; Thompson, C. J.; Turcu, R. V. F.; Miller, Q. R.; Chen, J.; Hu, J.; Hoyt, D. W.; Martin, P. F.; Ilton, E. S. et al. Clay Hydration/Dehydration in Dry to Water-Saturated Supercritical CO_2 : Implications for Caprock Integrity. *Energy Procedia* **2013**, *37*, 5443-5448.
25. Botan, A.; Rotenberg, R.; Marry, V.; Turq, P.; Noetinger, B. Carbon Dioxide in Montmorillonite Clay Hydrates: Thermodynamics, Structure and Transport from Molecular Simulation. *J. Phys. Chem. C* **2010**, *114*, 14962-14969.
26. Kadoura, A.; Nair, A. K. N.; Sun, S. Molecular Simulation Study of Montmorillonite in Contact with Variably Wet Supercritical Carbon Dioxide. *J. Phys. Chem. C* **2017**, *121*, 6199-6208.
27. Makaremi, M.; Jordan, K. D.; Guthrie, G. D.; Myshakin, E. M. Multiphase Monte Carlo and Molecular Dynamics Simulations of Water and CO_2 Intercalation in Montmorillonite and Beidellite. *J. Phys. Chem. C* **2015**, *119*, 15112-15124.
28. Rao, A.; Leng, Y. Effect of Layer Charge on CO_2 and H_2O Intercalations in Swelling Clays. *Langmuir* **2016**, *32*, 11366-11374.

29. Sena, M. M.; Morrow, C. P.; Kirkpatrick, R. J.; Krishnan, M. Structure, Energetics, and Dynamics of Supercritical Carbon Dioxide at Smectite Mineral-Water Interfaces: Molecular Dynamics Modeling and Adaptive Force Investigation of CO₂/H₂O Mixtures Confined in Na-Montmorillonite. *Chem. Mater.* **2015**, *27*, 6946-6959.
30. Yazaydin, A. O.; Bowers, G. M.; Kirkpatrick, R. J. Molecular Dynamics Modeling of Carbon Dioxide, Water and Natural Organic Matter in Na-Hectorite. *Phys. Chem. Chem. Phys.* **2015**, *17*, 23356-23367.
31. Cole, D. R.; Chialvo, A. A.; Rother, G.; Vlcek, L.; Cummings, P. T. Supercritical Fluid Behavior at Nanoscale Interfaces: Implications for CO₂ Sequestration in Geological Formations. *Philoso. Mag.* **2010**, *90*, 2339-2363.
32. Cole, D. R.; Ok, S.; Striolo, A.; Phan, A., Hydrocarbon Behavior at Nanoscale Interfaces. *Reviews in Mineralogy and Geochemistry* **2013**, *75*, 495-545.
33. Rother, G.; Ilton, E. S.; Wallacher, D.; Hauss, T.; Schaef, H. T.; Qafoku, O.; Rosso, K. M.; Felmy, A. R.; Krukowski, E. G.; Stack, A. G. et al. CO₂ Sorption to Subsingle Hydration Layer Montmorillonite Clay Studies by Excess Sorption and Neutron Diffraction Measurements. *Environ. Sci. Technol.* **2013**, *47*, 205-211.
34. Loganathan, N.; Yazaydin, A. O.; Bowers, G. M.; Kalinichev, A. G.; Kirkpatrick, R. J. Molecular Dynamics Study of CO₂ and H₂O Intercalation in Smectite Clays: Effect of Temperature and Pressure on Interlayer Structure and Dynamics in Hectorite. *J. Phys. Chem. C* **2017**, *121*, 24527-24540.
35. Loganathan, N.; Bowers, G. M.; Yazaydin, A. O.; Schaef, H. T.; Loring, J.; Kalinichev, A. G.; Kirkpatrick, R. J. Clay Swelling in Dry Supercritical Carbon Dioxide: Effects of Interlayer Cations on the Structure, Dynamics and Energetics of CO₂ Intercalation Probed by XRD, NMR and GCMD Simulations. *J. Phys. Chem. C* **2018**, *122*, 4391-4402.
36. Loganathan, N.; Bowers, G. M.; Yazaydin, A. O.; Kalinichev, A. G.; Kirkpatrick, R. J. Competitive Adsorption of H₂O and CO₂ in 2-Dimensional Nanoconfinement: GCMD Simulations of Cs- and Ca-Hectorites. *J. Phys. Chem. C* **2018**, *122*, 23460-23469.
37. Bowers, G. M.; Schaef, H. T.; Loring, J. S.; Hoyt, D. W.; Burton, S. D.; Walter, E. D.; Kirkpatrick, R. J. Role of Cations in CO₂ Adsorption, Dynamics and Hydration in Smectite Clays under In Situ Supercritical CO₂ Conditions. *J. Phys. Chem. C* **2017**, *121*, 577-592.
38. Schaef, H. T.; Loganathan, N.; Bowers, G. M.; Kirkpatrick, R.; Yazaydin, A. O.; Burton, S. D.; Hoyt, D. W.; Ilton, E. S.; Thanthiriwatt, K. S.; Dixon, D. A. et al. Tipping Point for Expansion of Layered Aluminosilicates in Weakly Polar Solvents: Supercritical CO₂. *ACS Appl. Mater. Interf.* **2017**, *9*, 36783-36791.
39. Bowers, G. M.; Loring, J. S.; Schaef, H. T.; Walter, E. D.; Burton, S. D.; Hoyt, D. W.; Cunniff, S. S.; Loganathan, N.; Kirkpatrick, R. J. Interaction of Hydrocarbons with Clays under Reservoir Conditions: In Situ Infrared and Nuclear Magnetic Resonance Spectroscopy and X-ray Diffraction for Expandable Clays with Variably Wet Supercritical Methane. *ACS Earth Space Chem.* **2018**, *2*, 640-652.
40. Giesting, P.; Guggenheim, S.; van Groos, A. F. K.; Busch, A. Interaction of Carbon Dioxide with Na-Exchanged Montmorillonite at Pressures to 640 bar: Implications for CO₂ Sequestration. *Int. J. Green. Gas Cont.* **2012**, *8*, 73-81.
41. Loganathan, N.; Yazaydin, A. O.; Kirkpatrick, R. J.; Bowers, G. M. Tuning the Hydrophobicity of Layer-Structure Silicates to Promote Adsorption of Non-Aqueous Fluids:

- Effects of F- and OH- Substitution on CO₂ Partitioning into Smectite Interlayers. *J. Phys. Chem. C* **2019**, *123*, 4848-4855.
42. Jin, Z.; Firoozabadi, A., Methane and Carbon Dioxide Adsorption in Clay-like Slit Pores by Monte Carlo Simulations. *Fluid Phase Equil.* **2013**, *360*, 456-465.
 43. Jin, Z.; Firoozabadi, A., Effect of Water on Methane and Carbon Dioxide Sorption in Clay Minerals by Monte Carlo Simulations. *Fluid Phase Equil.* **2014**, *382*, 10-20.
 44. Yang, N.; Liu, S.; Yang, X., Molecular Simulation of Preferential Adsorption of CO₂ over CH₄ in Na-montmorillonite Clay Mineral. *App. Surf. Sci.* **2015**, *356*, 1262-1271.
 45. Wang, Q.; Huang, L., Molecular Insight into Competitive Adsorption of Methane and Carbon Dioxide in Montmorillonite: Effect of Clay Structure and Water Content. *Fuel*, **2019**, *239*, 32-43.
 46. Chen, G.; Lu, S.; Liu, K.; Han, T.; Xu, C.; Xue, Q.; Shen, B.; Guo, Z. GCMC Simulations on the Adsorption Mechanisms of CH₄ and CO₂ in K-illite and their Implications for Shale Gas Exploration and Development. *Fuel* **2018**, *224*, 521-528.
 47. Zhang, J.; Clennell, M. B.; Liu, K.; Pervukhina, M.; Chen, C.; Dwhurst, D. N. Methane and Carbon Dioxide Adsorption on Illite. *Energy Fuels* **2016**, *30*, 10643-10652.
 48. Chong, L.; Myshakin, E. M. Molecular Simulations of Competitive Adsorption of Carbon Dioxide – Methane Mixture on Illitic Clay Surfaces. *Fluid Pha. Equil.* **2018**, *25*, 185-195.
 49. Wan, J.; Tokunaga, T. K.; Ashby, P. D.; Kim, Y.; Voltolini, M.; Gilbert, B.; DePaolo, D. J., Supercritical CO₂ Uptake by Nonswelling Phyllosilicates. *Proceedings of the National Academy of Sciences* **2018**, *115*, 873-878.
 50. Hwang, J.; Pini, R. Supercritical CO₂ and CH₄ Uptake by Illite-Smectite Clay Minerals. *Environ. Sci. Technol.* **2019**, DOI:10.1021/acs.est.9603638
 51. Loganathan, N.; Bowers, G. M.; Wakou, B. F. W.; Kalinichev, A. G.; Kirkpatrick, R. J.; Yazaydin, A. O. Understanding Methane/Carbon Dioxide Partitioning in Clay Nano- and Meso-pores with Constant Reservoir Composition Molecular Dynamics Modeling. *Phys. Chem. Chem. Phys.* **2019**, *21*, 6917-6924.
 52. Perego, C.; Salvalaglio, M.; Parrinello, M., Molecular Dynamics Simulation of Solutions at Constant Chemical Potential. *J. Chem. Phys.* **2015**, *142*, 144113.
 53. Karmakar, T.; Piaggi, P. M.; Perego, C.; Parrinello, M., A Cannibalistic Approach to Grand Canonical Crystal Growth. *J. Chem. Theory Comput.* **2018**, *14*, 2678-2683.
 54. Ozcan, A.; Perego C.; Salvalaglio, M.; Parrinello, M.; Yazaydin, O. Concentration Gradient Driven Molecular Dynamics: A New Method for Simulations of Membrane Permeation and Separation. *Chem. Sci.* **2017**, *8*, 3858-3865.
 55. Heffelfinger, G. S.; van Swol, F., Diffusion in Lennard-Jones Fluids Using Dual Control Volume Grand Canonical Molecular Dynamics Simulation (DCV-GCMD). *J. Chem. Phys.* **1994**, *100*, 7548.
 56. Hu, Y.; Ray, J. R.; Jun, Y-S. Na⁺, Ca²⁺, and Mg²⁺ in Brines Affect Supercritical CO₂-Brine-Biotite Interactions: Ion Exchange, Biotite Dissolution, and Illite Precipitation. *Environ. Sci. Technol.* **2013**, *47*, 191-197.

57. Farajzadeh, R.; Guo, H.; Winden, J.; Bruining, J. Cation Exchange in the Presence of Oil in Porous Media. *ACS Earth Space Chem.* **2017**, *1*, 101-112.
58. Rotenberg, B. Water in Clay Nanopores. *MRS Bulletin*, Cambridge University Press (CUP). **2014**, *39*, 1074-1081.
59. Altaner, S. M.; Weiss, C. A.; Kirkpatrick, R. J. Evidence from ^{29}Si NMR for the Structure of Mixed-Layer Illite/Smectite Clay Minerals. *Nature* **1988**, *331*, 699-702.
60. Lowenstein, W. The Distribution of Aluminium in the Tetrahedra of Silicates and Aluminates. *Am. Mineral.* **1954**, *39*, 92-96.
61. Plimpton, S. Fast Parallel Algorithms for Short-Range Molecular Dynamics. *J. Comp. Phys.* **1995**, *117*, (1), 1-19.
62. Hoover, W. G. Canonical Dynamics: Equilibrium Phase-Space Distributions. *Phys. Rev. A* **1985**, *31*, 1695-1697.
63. Cygan, R. T.; Liang, J.-J.; Kalinichev, A. G. Molecular Models of Hydroxide, Oxyhydroxide and Clay Phases and the Development of a General Force Field. *J. Phys. Chem. B* **2004**, *108*, 1255-1266.
64. Pouvreau, M.; Greathouse, J. A.; Cygan, R. T.; Kalinichev, A. G. Structure of Hydrated Gibbsite and Brucite Edge Surfaces: DFT Results and Further Development of ClayFF Classical Force Field with Metal-O-H Bending Terms. *J. Phys. Chem. C* **2017**, *121*, 14757 - 14771.
65. Pouvreau, M.; Greathouse, J. A.; Cygan, R. T.; Kalinichev, A. G. Structure of Hydrated Kaolinite Edge Surfaces: DFT Results and Further Development of ClayFF Classical Force Field with Metal-O-H Angle Bending Terms. *J. Phys. Chem. C* **2019**, *123*, 11628 -11638.
66. Cygan, R. T.; Romanov, V. N.; Myshakin, E. M. Molecular Simulation of Carbon Dioxide Capture by Montmorillonite Using an Accurate and Flexible Force Field. *J. Phys. Chem. C* **2012**, *116*, 13079-13091.
67. Martin, M. G.; Siepmann, J. I. Transferable Potentials for Phase Equilibria. 1. United-Atom Description of n-Alkanes. *J. Phys. Chem. B* **1998**, *102*, 2569-2577.
68. Plimpton, S. J.; Pollock, R.; Stevens, M. J., Particle-Mesh Ewald and rRESPA for Parallel Molecular Dynamics Simulations: Proceedings of the Eighth SIAM Conference on Parallel Processing for Scientific Computing, Minneapolis, Minnesota, 1997.
69. Tribello, G. A.; Bonomi, M.; Branduardi, D.; Camilloni, C.; Bussi, G.; Plumed 2: New Feathers for an Old Bird. *Comput. Phys. Commun.* **2014**, *185*, 604-613.
70. Peng, D. Y.; Robinson, D. B. A New Two-Constant Equation of State. *Ind. Eng. Chem. Fundam.* **1976**, *15*, 59-64.
71. Criscenti, L. J.; Cygan, R. T., Molecular Simulations of Carbon Dioxide and Water: Cation Solvation. *Environ. Sci. Technol.* **2013**, *47*, 87-94.
72. Wang, J.; Kalinichev, A. G.; Kirkpatrick, R. J.; Cygan, R. T. Structure, Energetics and Dynamics of Water Adsorbed on the Muscovite (001) Surface: A Molecular Dynamics Simulation. *J. Phys. Chem. B* **2005**, *109*, 15893-15905.

73. Chong, L.; Myshakin, E. M. The Effect of Residual Water Content on Preferential Adsorption in Carbon Dioxide - Methane – Illite Clay Minerals: A Molecular Simulation Study. *Fluid Pha. Equil.* **2020**, *504*, 112333.

Figures

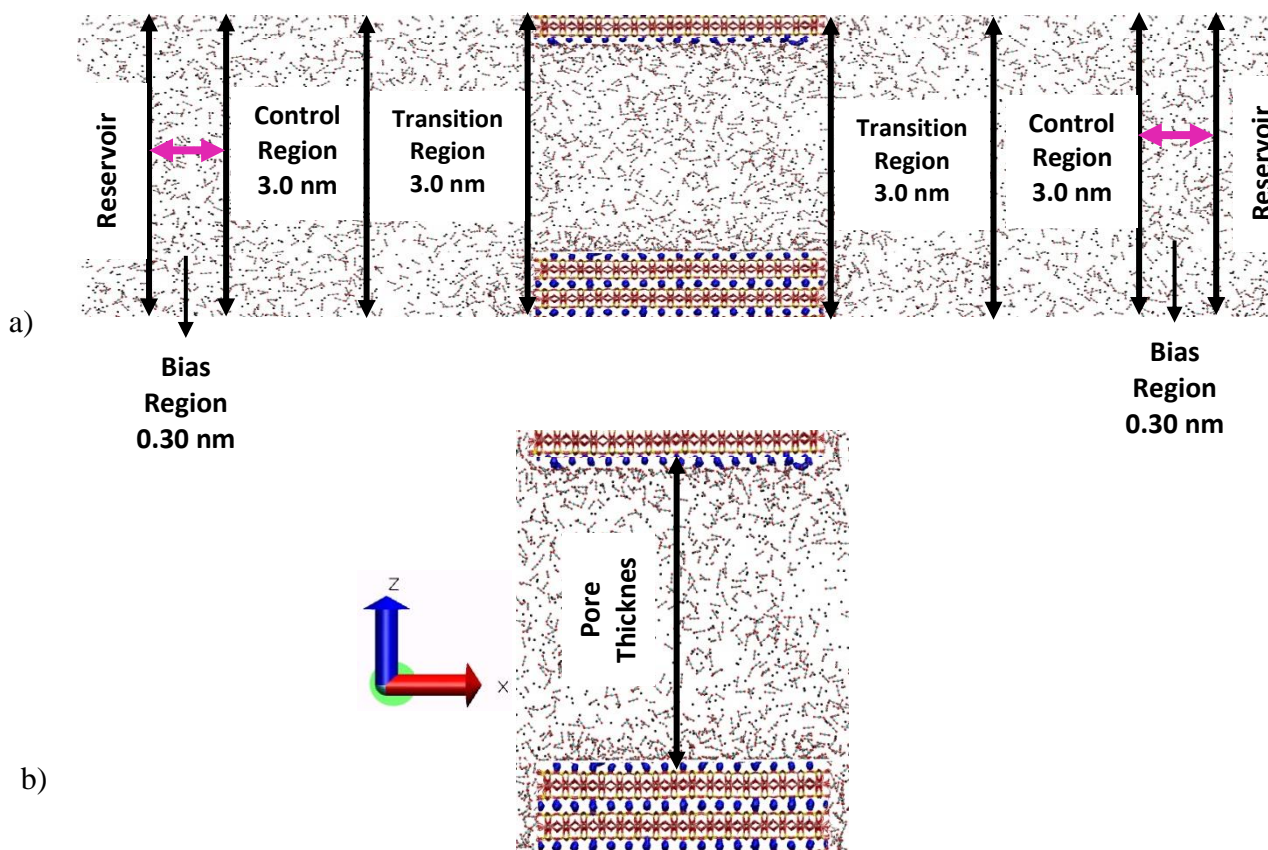


Figure 1: Schematic representation of the simulation cells used in the Constant Reservoir Composition Molecular Dynamics (CRC-MD) calculations used here to study CO_2/CH_4 partitioning into pores bounded by illite basal surfaces. a) The full simulation cell showing the different regions of the models. b) Enlarged image of the silt-like pore and finite size illite T-O-T layers. Color code: Si - Yellow; O - Red; Al - Pink; H - White; Cations (K^+/Na^+) - Blue; C_{CO_2} - Cyan; C_{CH_4} - Black. Substrate atoms are represented using sticks and the CO_2 and CH_4 molecules and metal ions are represented by balls. Pink arrows represent

the bias forces used to control the fluid composition in the control regions. The directions of X and Z axes are indicated by the arrows in the lower left.

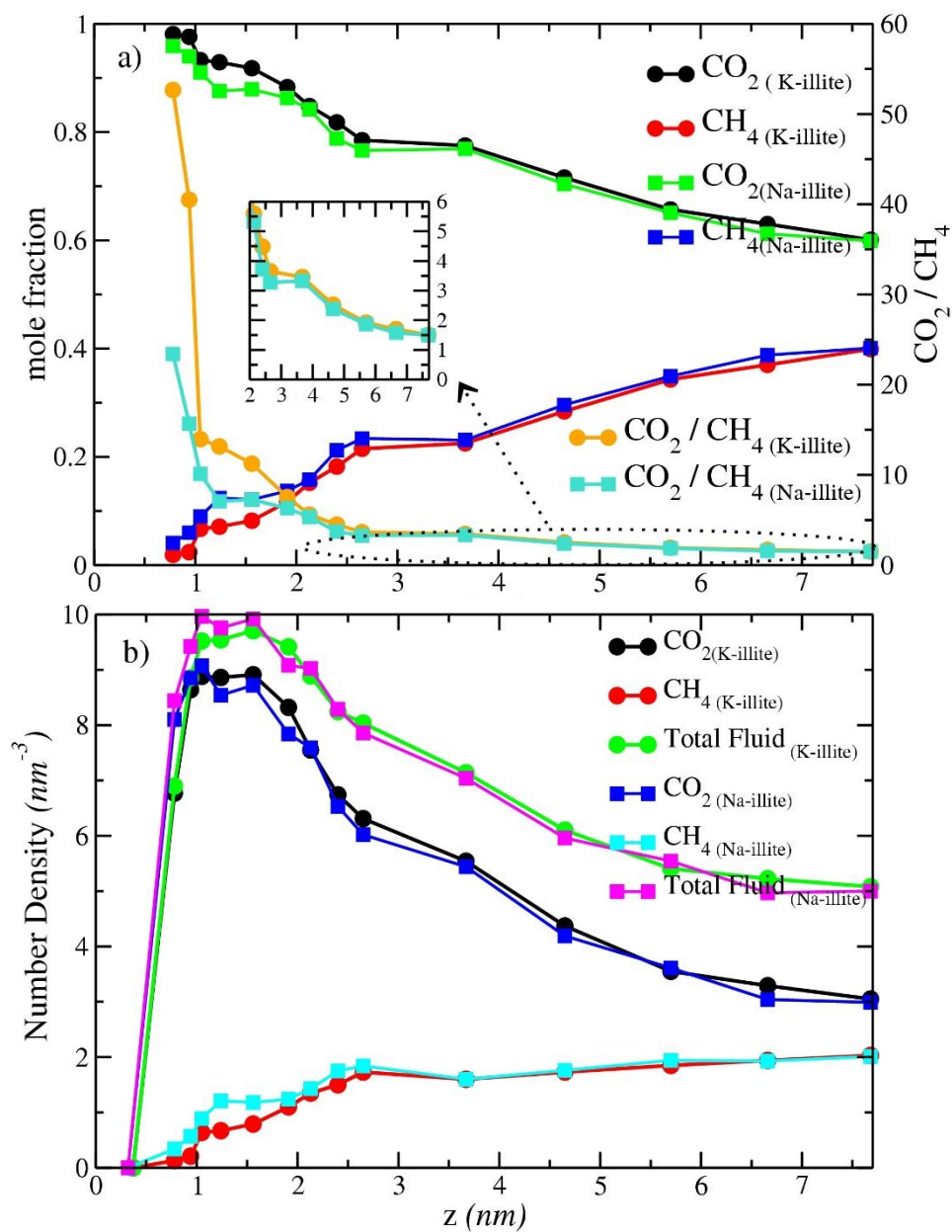
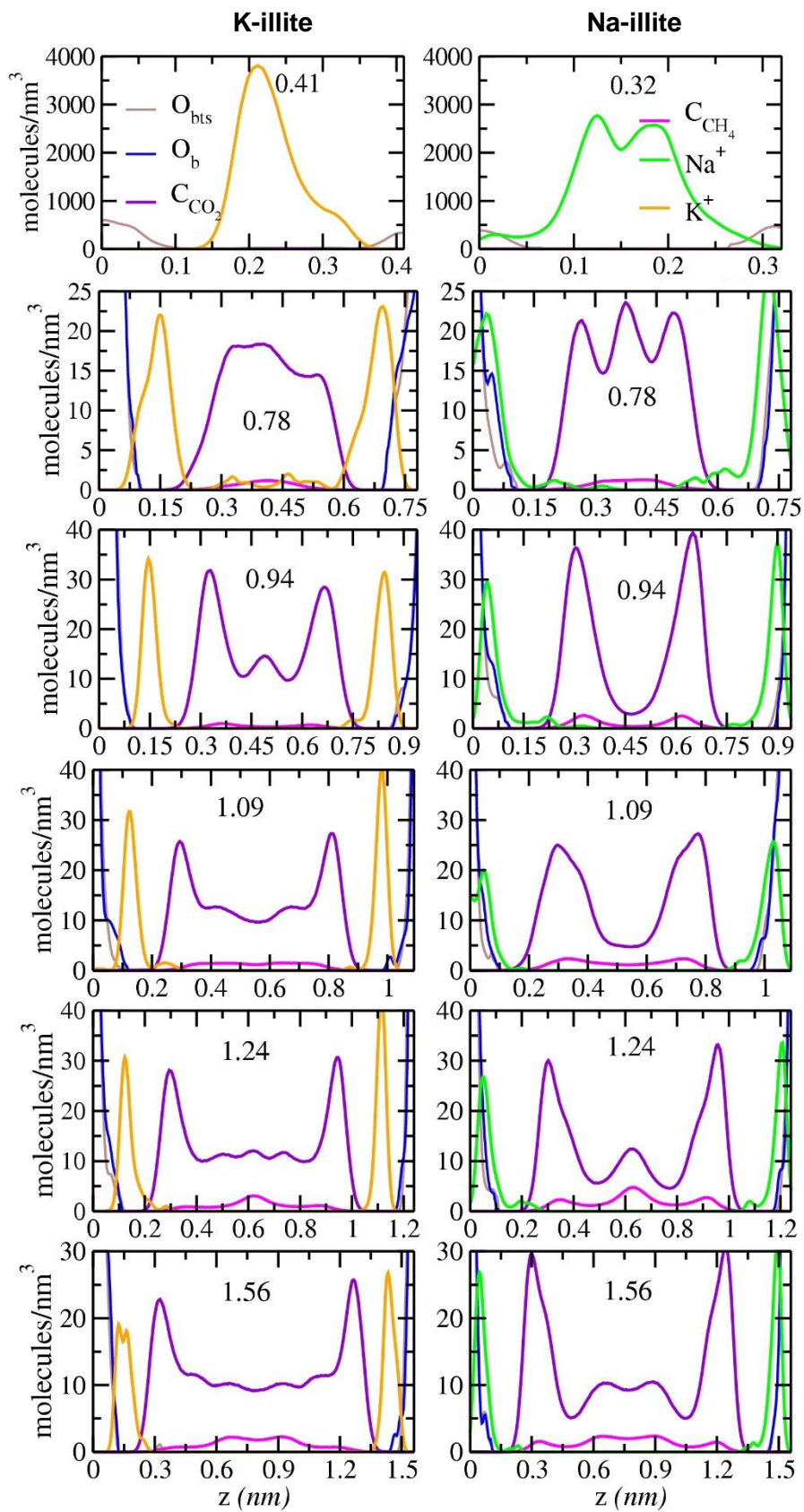


Figure 2. a) Computed mole fractions of CO_2 and CH_4 molecules and the CO_2/CH_4 ratios with K^+ and Na^+ as the exchangeable cation on the pore surfaces as functions of pore thickness for pores bounded by (001) surfaces. b) Number density of the fluid species confined within these pores as functions of pore thickness.



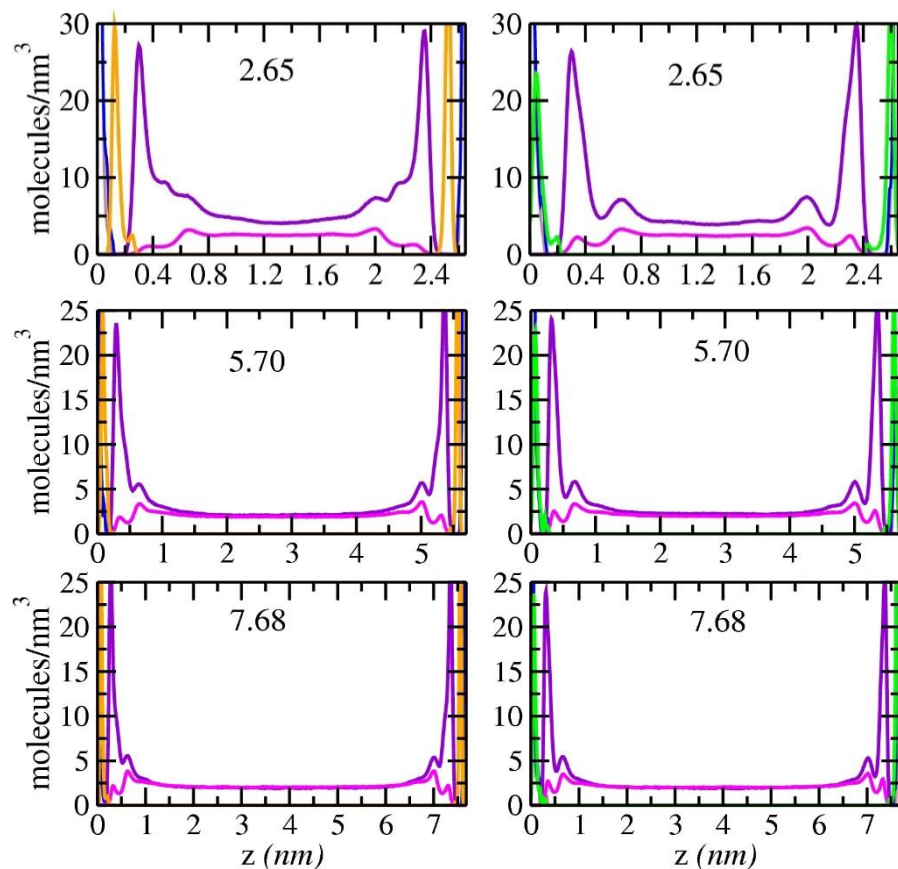


Figure 3. Computed probability density profiles (PDPs) of metal cations K^+ (orange), Na^+ (green), C_{CO_2} (violet) and C_{CH_4} (magenta) as functions of distance normal to the (001) surfaces of illite with varying pore thicknesses. The vertical brown and blue lines represent the positions of the oxygen atoms of the illite basal surfaces coordinated to tetrahedral Si sites (O_b - blue) and tetrahedral Al sites (O_{bts} - brown). Left and right columns represent the PDPs of models with exchangeable K^+ and Na^+ on the (001) surfaces, respectively.

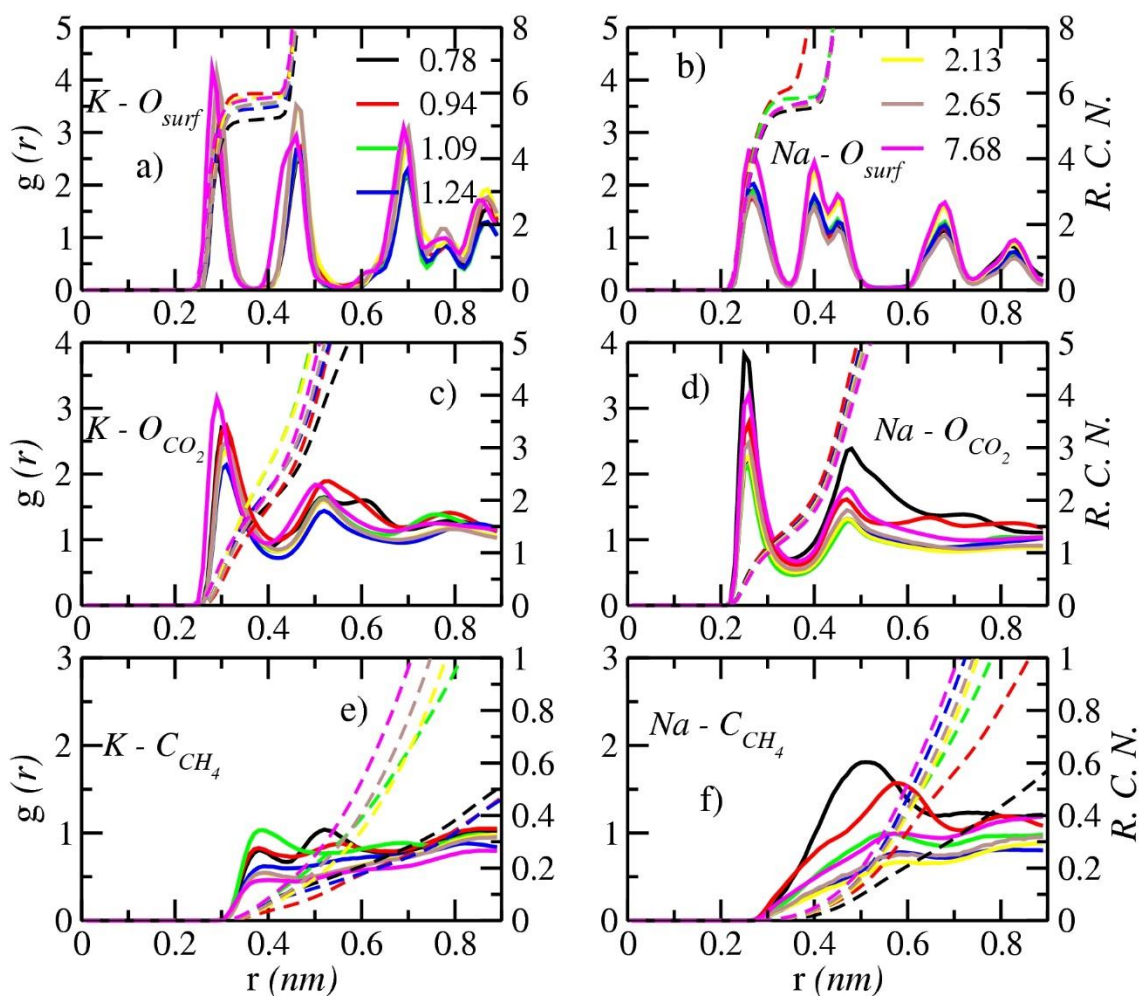


Figure 4. Radial distribution functions (RDFs; solid lines) and the corresponding running coordination numbers (RCNs; dashed lines) of the indicated exchangeable surface cations (K^+ and Na^+) with the fluid species and the basal oxygen atoms of the illite (001) surface at different pore thickness.

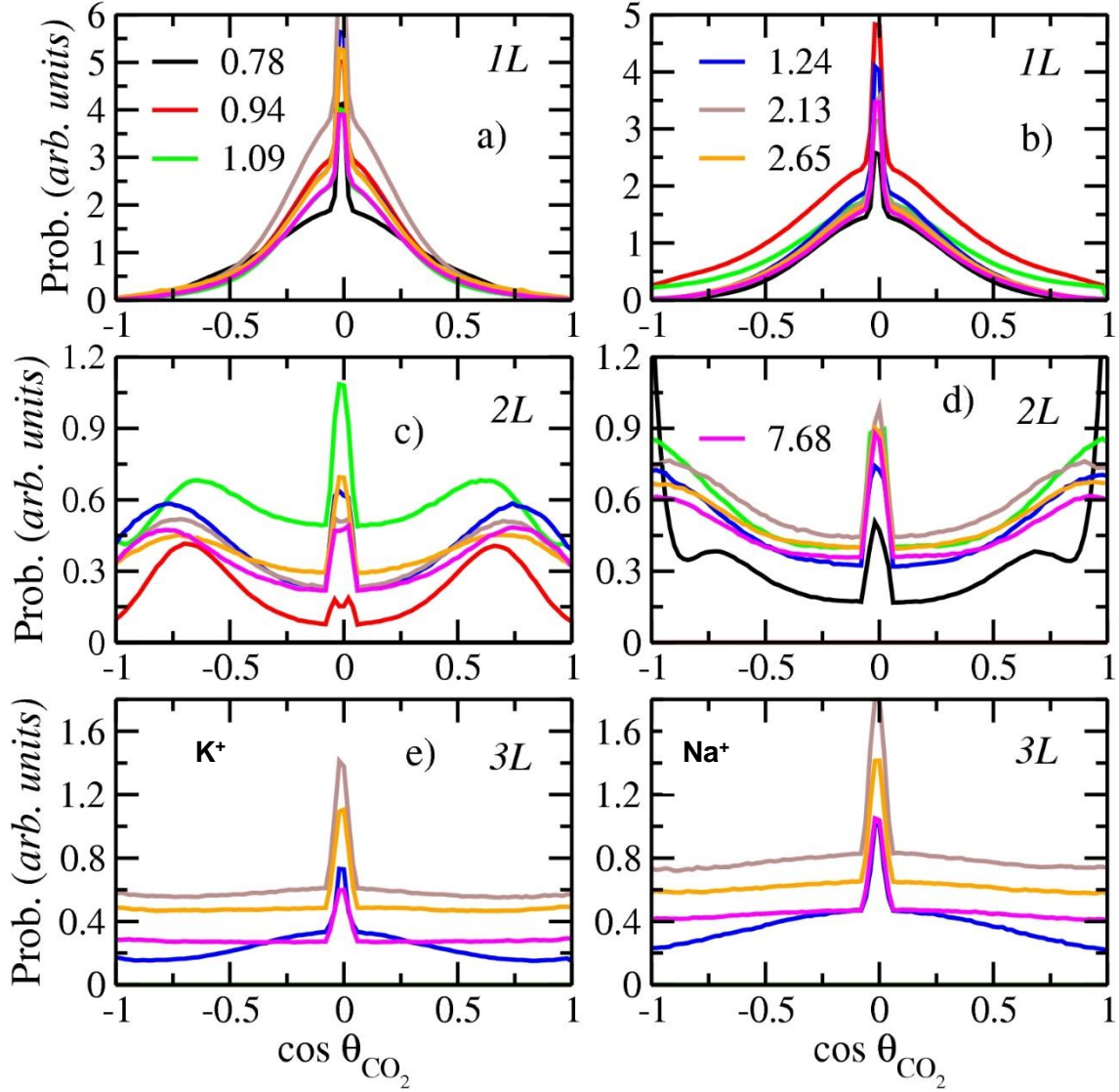


Figure 5. Computed angular distribution of C_{CO_2} molecules in each of the first three layers near the illite (001) basal surfaces as functions of pore thickness with K^+ (left) and Na^+ (right). $\cos \theta_{\text{CO}_2}$ is the cosine of the angle between the O-O vector of CO_2 molecules and the normal to the (001) surface.

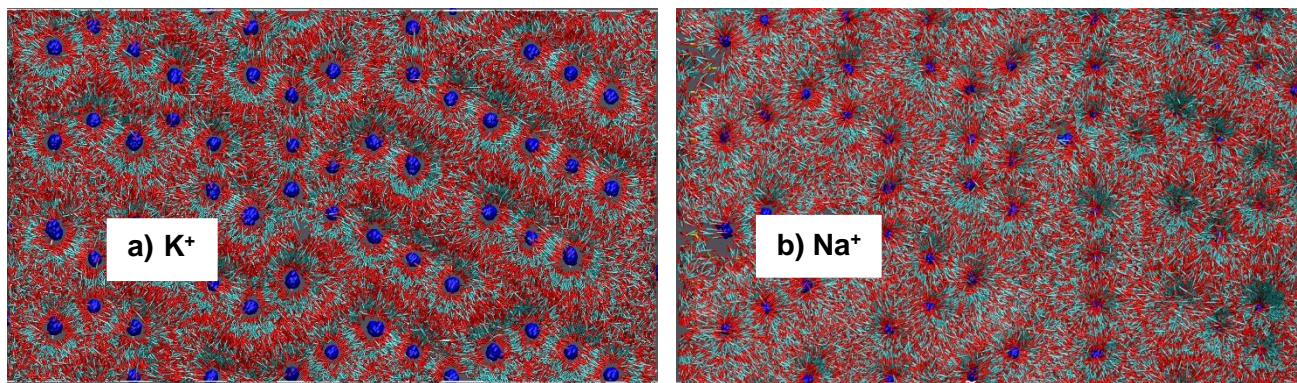


Figure 6. Pictorial representation of relationships between the CO₂ molecules in the first fluid layer (0.0 to 0.35 nm from the surface) with a) K⁺ (left) and b) Na⁺ (right) at the largest pore thickness studied (7.68 nm). Each image is the sum of 2000 frames in the MD production run and illustrates the structural effects of the greater affinity of CO₂ for K⁺ than Na⁺. Color code: red and cyan sticks represent the O and C of CO₂ respectively; the exchangeable cations are in shown as blue balls.

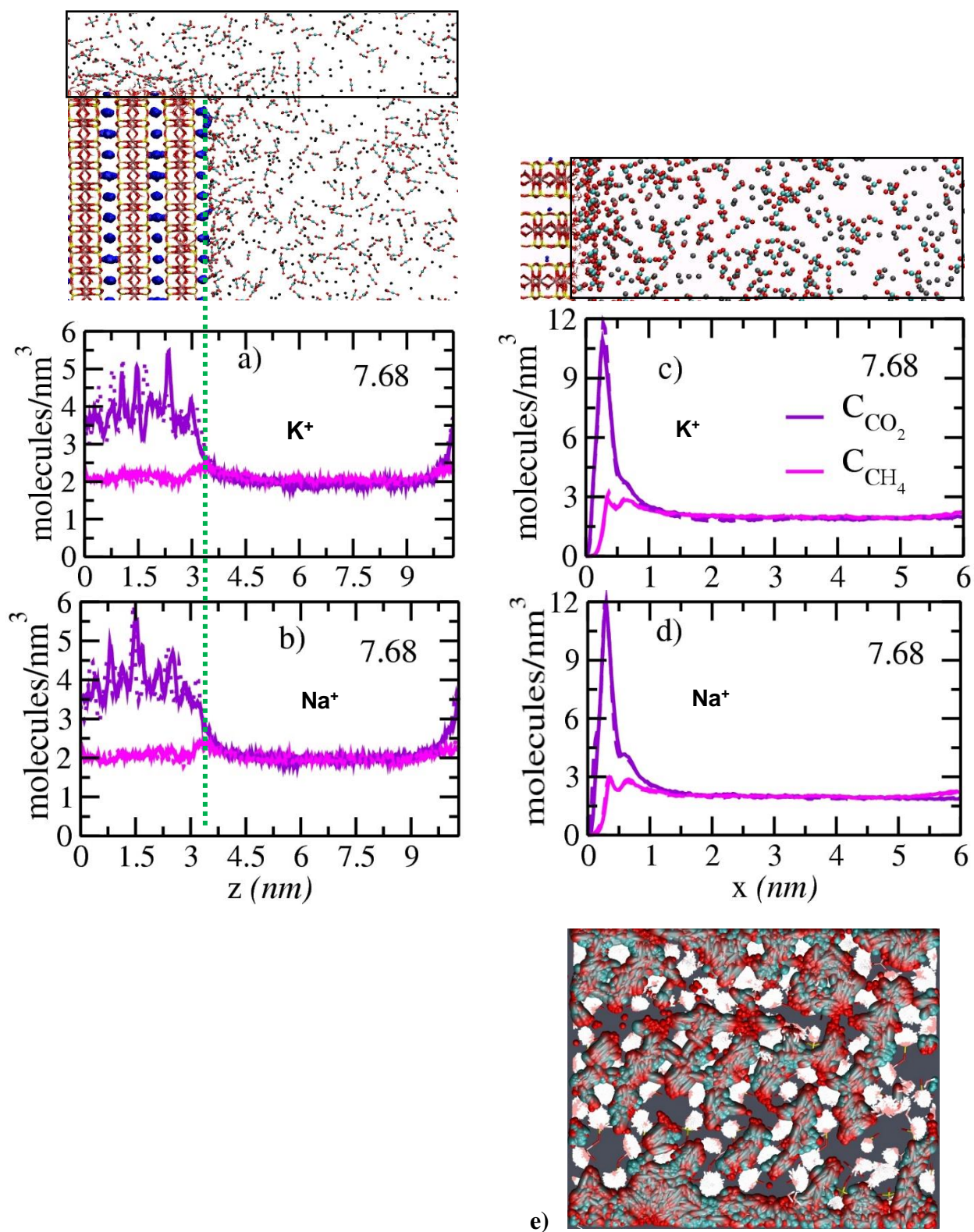


Figure 7. Computed PDP's of C_{CO_2} (violet) and C_{CH_4} (magenta) near the broken and protonated (010) surfaces with K^+ and Na^+ . The left column represents the average concentrations

within 1.50 nm of the surfaces plotted parallel to them for the pore thicknesses shown at the top of the box. a) K^+ and b) Na^+ . Solid and dashed lines represent the distributions on the left and right sides of the illite models. Green dotted lines in a) and b) represent the plane of basal oxygen atoms of the (010) surface. The right column shows the distributions normal to the (010) surfaces. c) K^+ and d) Na^+ . e) The adsorption environments of CO_2 molecules in the shoulder region near the protonated (010) surface (0.0 to 0.2) nm from the surface, comparable to Figure 6. Red and white sticks represent the protonated edges of the (010) surfaces. CO_2 molecules are represented in red (O) and cyan (C).

TOC Graphic

